RSC Advances

PAPER

View Article Online
View Journal | View Issue

Cite this: *RSC Adv.*, 2018, **8**, 24355

Effect of ionic size compensation by Ag^+ incorporation in homogeneous Fe-substituted ZnO: studies on structural, mechanical, optical, and magnetic properties

Gaurav Bajpai,[a] Tulika Srivastava,[a] N. Patra,[c] Igamcha Moirangthem,[d] S. N. Jha,[c] D. Bhattacharyya,[c] Sk Riyajuddin,[e] Kaushik Ghosh,[e] Dharma R. Basaula,[f] Mahmud Khan,[f] Shun-Wei Liu,[g] Sajal Biring*[g] and Somaditya Sen*[abg]

Received 19th March 2018
Accepted 21st June 2018

DOI: 10.1039/c8ra02393j

rsc.li/rsc-advances

Substituting an ion of different size from that of the host element introduces lattice strain and defects. However, this mismatch may be significantly reduced by substituting an additional ion with a compensating size relative to the dopant. Such a double substitution might offer better solubility irrespective of the local distortions as well as the formation of defects in the valence states. Fe-substituted ZnO has been widely reported with conflicting results primarily arising from lack of chemical and structural homogeneity originating from preparation techniques, compositional fluctuations, and equivocal comprehension of actual solubility limits of the dopants. In this study, Ag ion has been incorporated in Fe-substituted ZnO to compensate the ionic size of $Zn_{1-x}[Fe_{0.8}Ag_{0.2}]_xO$ ($0 \leq x \leq 0.03125$) by determining the solubility limit of the homogeneous material and their corresponding structural, mechanical, optical and magnetic properties have been investigated thoroughly. Co-substitution rearranges the lattice and leads to better crystal structures with tunable properties related to the amount of substitution.

Introduction

Zinc oxide (ZnO) is a II–VI group semiconductor with a direct band gap energy of 3.37 eV. It has a large exciton binding energy of 60 meV at room temperature. It has attracted much attention due to its unique properties and various technological applications. Applications include optics, optoelectronics, magneto-electronics, highly efficient blue LEDs and microwave devices.[1–5] Nanostructured ZnO materials can also behave as a dilute magnetic semiconductor (DMSs). This has attracted great attention in the design of devices with spin based electronics (spintronics).[1] There are many reports on ZnO doped with transition metal (TM) ions which point to many applications including room temperature ferromagnetic semiconductor nanomaterials and room temperature nano-lasers.[6–10] Dietl *et al.*[11] and Sato *et al.*[12] indicate the possibility of room temperature ferromagnetism (RTFM) in transition metal doped ZnO, and there has been a great deal of research work carried out on ZnO based dilute magnetic semiconductors (DMS). There have been many claims from numerous researches that there is a presence of ferromagnetism in transition metals (Co, Mn, Fe, Ni, Cr, *etc.*) doped ZnO using defect related mechanisms, hole mediated exchange interactions, secondary phases, bound magnetic polarons (BMPs), clusters, organic capping agents, synthesis methods *etc.* at low and high Curie temperatures.[13–20] However, others have claimed the contrary.[21,22] Ferromagnetism in ZnO without doping of transition metal ions has also been discussed.[23] Magnetic properties of multiple ions doped (or) co-doped ZnO nanomaterials are also studied.[24,25] However, the real origin of ferromagnetism is still controversial as magnetism appears in pure ZnO, TM doped ZnO and non-TM doped ZnO.[26]

There are various types of physical and chemical methods for synthesizing samples such as simple vapor transport and chemical co-precipitation method,[27] solid state reaction method,[28] radio-frequency (rf) magnetron sputtering technique,[29] facile low temperature synthesis,[30] sol–gel method,[31–33] *etc.* Among these methods, sol–gel method is a simple, inexpensive and high yield method providing uniform homogeneous powders. In the present work, we have chosen Fe-substituted ZnO, $Zn_{1-x}Fe_xO$ with $0 < x < 0.03125$ (ZFO), to

[a]*Metallurgical Engg. and Material Sciences, Indian Institute of Technology Indore, India. E-mail: sens@iiti.ac.in*
[b]*Department of Physics, Indian Institute of Technology Indore, India*
[c]*Atomic & Molecular Physics Division, Bhabha Atomic Research Centre, Mumbai, India*
[d]*Amity Institute of Nanotechnology, Noida, U.P., India*
[e]*Institute of Nano Science and Technology, Mohali, Punjab, India*
[f]*Department of Physics, Miami University, Oxford, Ohio 45056, USA*
[g]*Electronic Engg., Ming Chi University of Technology, New Taipei City, Taiwan. E-mail: biring@mail.mcut.edu.tw*

investigate the existence of magnetism in a homogenously substituted material. Silver (Ag) acts as an excellent neutralizer of native defect states in ZnO, thereby enhancing optical properties.[27] In general, Fe-substituted ZnO lattice strain keeps on increasing due to growing differences in crystalline sizes of Zn and Fe. Also, there is a charge difference between the dopant and the host. Attempts are being made to minimize native defect states by substitution with Ag in a Fe-substituted ZnO lattice. A $Zn_{1-x}[Fe_{0.8}Ag_{0.2}]_xO$ (ZFAO), with $0 \leq x \leq 0.03125$, series is synthesized using a similar sol–gel method. There are lots of conflicting results about solubility limits of Fe doped ZnO nanomaterials. Some authors reported solubility limit of Fe in ZnO to be less than 4% using different methods.[34,35] Hence, this study limits substitution to $x \sim 0.03125$. Structural, local structural and magnetic properties have been investigated to rule out impurity and homogeneity factors.

Experimental

$Zn_{1-x}Fe_xO$ (ZFO) and $Zn_{1-x}[Fe_{0.8}Ag_{0.2}]_xO$ (ZFAO) ($0 \leq x \leq 0.03125$) nanoparticles have been synthesized by sol–gel process followed by solid state sintering. The choice of sol–gel route was because dopant/substituent elements can be distributed in a modified lattice in different concentrations in different regions due to improper mixing of constituent elements. This concentration gradient in the lattice will give rise to different functionalities at different regions. By mixing the constituent elements in the liquid phase and then letting them react, we have ensured the formation of the desired homogeneous solid solution.

Dissolving ZnO powder (zinc oxide, Alfa Aesar, purity 99.9%) in HNO_3 (Alfa Aesar, purity 70%) and adding appropriate number of dopants $AgNO_3$ (silver nitrate, Alfa Aesar, purity 99.9%) and $Fe(NO_3)_3 \cdot 9H_2O$ (ferric nitrate nonahydrate, Alfa Aesar, purity 99.9%), a homogeneous solution molar ratio of Zn : Fe (128 : 1) and molar ratio of Zn : Fe : Ag (64 : 4: 1) was prepared by prolonged stirring. A solution of citric acid and glycerol were added to serve as fuel and gelling agent. Burnt gels were de-carbonized and denitrified at 450 °C for 6 h to get fine ZFO and ZFAO nanoparticles. These nanoparticles were further annealed at 600 °C for 2 h. From previous experience, a change in slope of Thermo Gravimetric Analysis (TGA) plots of as prepared samples was observed at ~450–550 °C. The flatness of TGA data beyond this temperature did not vary for most of the samples, irrespective of the dopant/substituent. It is some internal atomic rearrangement, may be related to reduction of crystal defects and improved crystal quality that stabilizes structure beyond 550 °C. Hence, to avoid such issues of instability, a choice of annealing the samples at 600 °C was taken. It has also been reported that the intensity of the UV peak becomes stronger after annealing at ~600 °C.[36–38] Also oxygen defects related to green emission reduces, indicating much better crystal quality.[39,40] Similar results were reiterated on previously reported series from this lab. Hence, samples were annealed at 600 °C to maintain uniformity in crystal quality of all samples.

X-ray diffraction (XRD) patterns of samples were obtained using a Bruker D2 Phaser X-ray diffractometer. Lattice parameters were calculated from Rietveld refinement of XRD data using GSAS Software. Surface morphology and chemical homogeneity have been investigated by Field Emission Scanning Electron Microscopy and Energy Dispersive X-ray Spectroscopy using a Carl Zeiss FESEM Supra-55 Spectrometer.

XANES and EXAFS measurements of samples have been carried out at room temperature at Energy Scanning EXAFS beamline (BL-9) at INDUS-2 Synchrotron source (2.5 GeV, 100 mA), Raja Ramanna Centre for Advanced Technology (RRCAT), Indore, India.[41,42] Photon energy range of the beamline is 4–25 keV. Beamline optics consists of a Rh/Pt coated collimating meridional cylindrical mirror used for collimation of beam. Collimated beam is monochromatized by a Si (111) ($2d = 6.2709$ Å) double crystal monochromator (DCM). The Rh/Pt mirror is used prior to the DCM for higher harmonic rejection. Second crystal of DCM is a sagittal cylindrical crystal, used for horizontal focusing of beam. Another Rh/Pt coated bendable post mirror facing downwards is used for vertical focusing of beam at sample position. EXAFS measurements at Zn K-edge (9659 eV) were performed in transmission mode while those at Fe K-edge (7112 eV) were performed in fluorescence mode. It should be noted that measurements at Ag K-absorption edge (25.514 keV) could not be done due to limitations of the above beamline (works in the range of 5–25 keV).

For data collection in transmission mode two ionization chambers, each of 30 cm length have been used. First and second ionization chambers measure incident flux (I_0) and transmitted flux (I_t) 70–90%, respectively. X-ray absorption coefficient is determined using relation, $\mu = \ln(I_0/I_t)$. Appropriate gas mixtures with optimized pressures were chosen to achieve 10–20% and 70–90% absorption in first and second ionization chambers, respectively, to improve signal to noise ratio. Rejection of higher harmonics of X-ray source was performed by 30% detuning of second crystal of DCM using piezo motor. To obtain a proper edge jump, samples of appropriate weight were taken in powder form and were pelletized (diameter ~ 15 mm) by mixing with 100 mg cellulose and were kept in a Teflon tape. For EXAFS measurement in fluorescence mode, samples were placed at 45° to incident X-ray beam. Fluorescence signal (I_f) is detected using a Si drift detector placed at 90° to incident beam. First ionization chamber was placed prior to sample to measure incident beam (I_0). X-ray absorption coefficient of sample was determined by $\mu = (I_f/I_0)$, and spectra were obtained as a function of energy by scanning a specific energy range using an appropriate monochromator.

Vickers micro-hardness measurements were carried out at room temperature using a digital micro-hardness tester (VHL) on pellets sintered at 600 °C. Load ~0.249–4.9 N was applied for 10 seconds. A diamond pyramid with square bottom with 136° angle between opposite surfaces has been used as indenter.

Optical transmittance data was obtained using Shimadzu UV-vis spectrometer (model UV-2600). Room-temperature photoluminescence (PL) of ZFO and ZFAO samples was performed using Dongwoo-Optron DM 500i spectrometer (excitation wavelength 325 nm).

Magnetic field dependent magnetization of the samples was examined using a Quantum Design Physical Property Measurement System (PPMS).

Results and discussion

Structural analysis

FESEM analysis. FESEM images show agglomerated spherical nanoparticles [Fig. 1(a) and (b)]. Particle size was also calculated using Image J software and the particle growth is not uniform and the particle size was found to be vary from 50–82 nm size. It seems that Ag addition in ZFAO has resulted in loss of sharper edges of the crystallites as compared to ZFO. Table 1 represents particle size with substitution. Fig. 1(c) and (d) highlight the typical EDX spectra taken from 0.0156 ZFO & 0.0156 ZFAO samples. The chemical analysis of ZFO & ZFAO nanoparticles for $x = 0.0156$ measured by EDX analysis shows the presence of Zn, O, Fe and Ag only.

XRD analysis. X-ray Diffraction (XRD) patterns of samples are shown in Fig. 2(a) and (b). It reveals hexagonal phase of ZFO and ZFAO nanoparticles for $0 < x < 0.03125$. No secondary phases are observed. Fig. 3(a) and (b) show Rietveld refinement of 0.0156 ZFO and 0.0156 ZFAO respectively.

Rietveld refinement of XRD data using GSAS software reveals that lattice parameters, '*a*' and '*c*' decrease in ZFO with increasing *x*, but increase in ZFAO samples [Fig. 4(a)]. Using Scherrer formula,

Table 1 Particle sizes of all samples from FESEM

Sample	Particle Size (nm)	Sample	Particle Size (nm)
Pure ZnO	50.158 ± 0.00021	Pure ZnO	50.158 ± 0.00021
0.0078 ZFO	74.256 ± 0.00034	0.0078 ZFAO	70.235 ± 0.00037
0.0156 ZFO	82.671 ± 0.00056	0.0156 ZFAO	65.354 ± 0.00037
0.0234 ZFO	72.245 ± 0.00048	0.0234 ZFAO	59.738 ± 0.00061
0.03125 ZFO	68.164 ± 0.00058	0.03125 ZFAO	55.535 ± 0.00029

$$D = \frac{18\,000(K\lambda)}{\pi L_x} \quad (1)$$

(where $K = 1$ is a constant), average crystallite sizes of ZFO and ZFAO nanoparticles were found to increase from 45 nm to 80 nm and thereafter decrease for higher substitution [Fig. 4(b)].

Lattice strain (S) was calculated from refinement parameters using formula equation:

$$S = \frac{\pi}{18\,000} L_y \quad (2)$$

In ZFAO, strain initially decreases for $x < 0.0156$ but increases for $x > 0.0156$. However, in ZFO, strain initially decreases for $x < 0.0078$ but thereafter increases.

For lower substitution $x < 0.0156$, strain decreases and thereafter increases for $x > 0.0156$. As a result of decreasing and

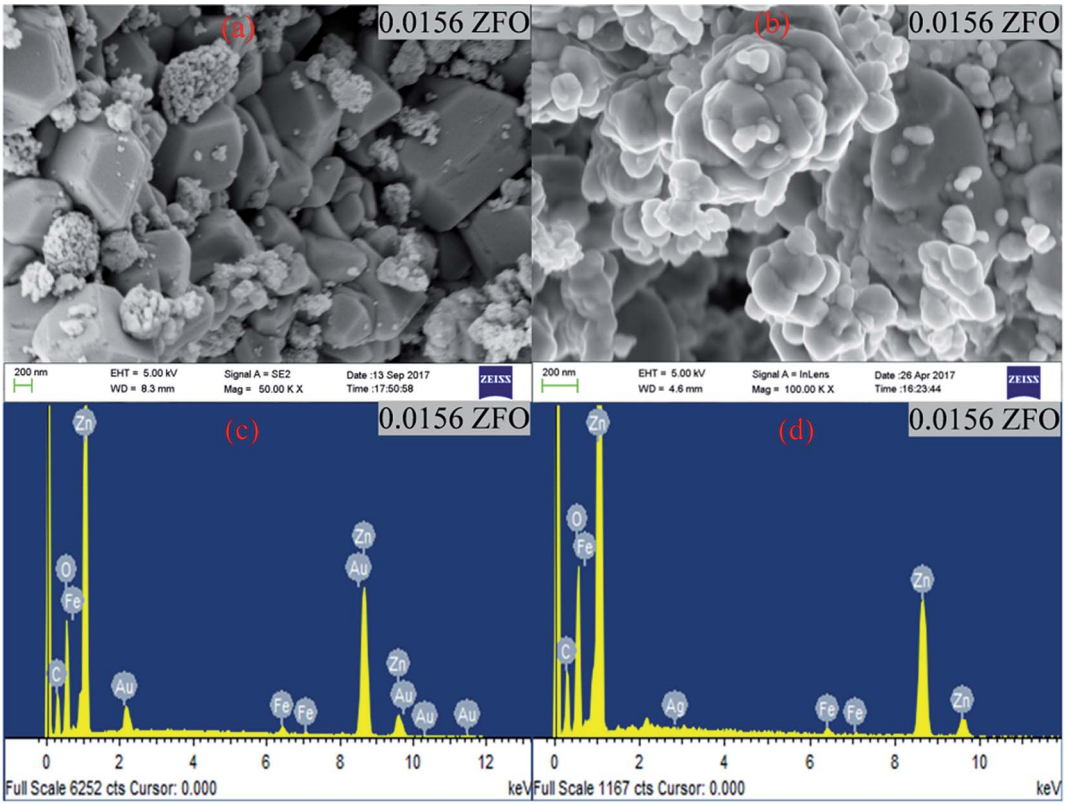

Fig. 1 (a) and (b) FESEM images of 0.0156 ZFO & 0.0156 ZFAO, (c) and (d) EDX of 0.0156 ZFO & 0.0156 ZFAO.

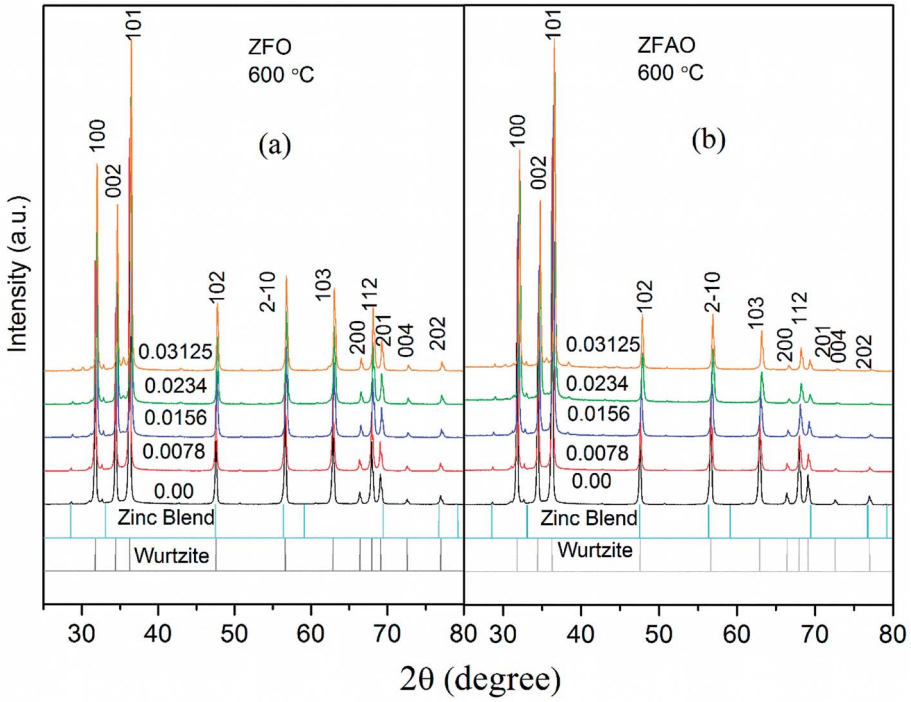

Fig. 2 (a) and (b) XRD patterns of ZFO & ZFAO.

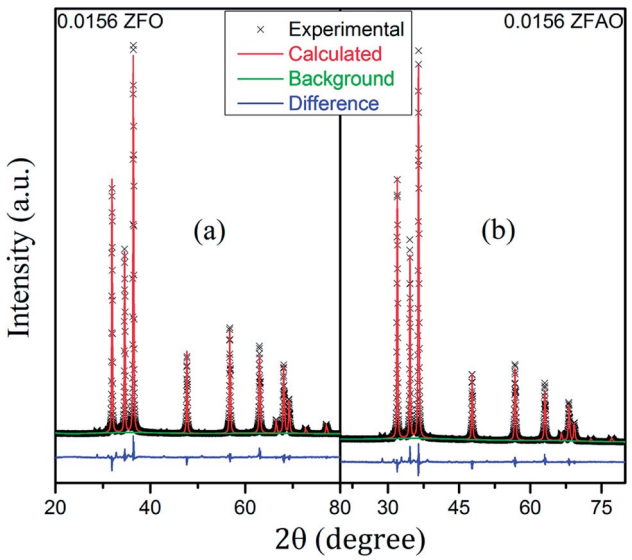

Fig. 3 (a) and (b) Rietveld refinement of 0.0156 ZFO and 0.0156 ZFAO.

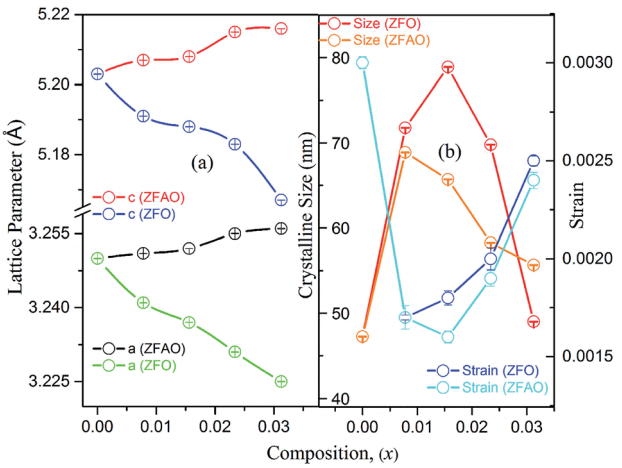

Fig. 4 (a) Lattice parameter of ZFO & ZFAO, (b) crystalline size & strain of ZFO & ZFAO.

increasing strain in the lattice crystallinity is affected. A longer range of structural order is expected for a better crystalline sample with lesser strain.[43] Hence a reverse trend of strain and crystallite size is observed in the samples. It is to be noted that strain reduces and then enhances both for ZFAO and ZFO. Note that the ratio of Fe^{3+} to Ag^{+} is ~4 : 1. Hence 3 out of 4 Fe ions atoms will add to the extra charge of the lattice. This will invite more oxygen to the lattice. The latent oxygen defects will be annihilated by such addition initially. But growing oxygen population will then add up to generation of strain for higher substitution after neutralization of latent O defects. O interstitial starts to form. This will create extra pressure leading to a strained lattice. The increased pressure in ZFAO results in the increase of lattice parameters in all directions in spite of ionic size compensation by Fe/Ag combination. However in ZFO samples, this cannot happen due to the size difference of Fe^{3+}(IV) (~0.63 Å) and Zn^{2+}(IV) (~0.74 Å). In ZFO samples the latent oxygen defect compensation is faster and starts at x = 0.0078.

X-ray absorption near edge structure (XANES)

Zn K-edge. Quantitative comparison of absorption features at Zn K-edge (9659 eV) of normalized XANES spectra ($\mu(E)$ *vs.* E)

spectra of ZFO and ZFAO samples was performed along with Zn metal foil (Zn^0) and standard ZnO (Zn^{2+}) [Fig. 5(a) and (c)]. Normalization of absorption spectra was done employing a standard edge step normalization process.[44] Zn-edges for both ZFO and ZFAO remain little below standard ZnO (Zn^{2+}) sample. A hump-like feature appears at ~9662 eV in ZFO samples but is not observed in ZFAO. Derivatives of the edge provide two maxima corresponding to two ionic states of Zn in ZFO. These two states can be referred to as Zn^{2+} and $Zn^{+(2-\delta)}$, where δ is a small addition or deficit. Compared to ZFO, ZFAO samples show less deviation from ZnO. These observations clearly indicate that in the substituted samples there is some presence of charge imbalance which was compensated by co-substitution. The presence of Fe^{3+} ions in the lattice may attract more oxygen towards the Fe^{3+} ions. As a result in the vicinity of a Fe^{3+} ion, the Zn ions may experience lesser electronic contribution from the O ions. Hence, a $(2-\delta)$ state is possible. On the other hand a Zn ion not in the neighborhood of a Fe ion will experience a different electronic contribution from the O ions. This may be the reason for the existence of the hump like feature in ZFO samples. In ZFAO this is somewhat reduced due to the presence of Ag^+ ions.

Significant increase in white line intensity labeled as point 'B' for both ZFO/ZFAO samples have been observed compared to that of pure ZnO. This mainly arises due to the charge transfer of Fe and Ag, suggesting significant increase in oxygen vacancies/holes near Zn sites due to substitution which is also reflected from EXAFS results.[45]

Fe K-edge. Normalized XANES absorption Fe K-edge (B) of ZFO and ZFAO samples reveals higher oxidation states than Fe^{2+} [Fig. 5(b) and (d)]. Pre-edge peak arises due to intermixing of Fe/Zn 3d and O 4p states. Insets [Fig. 5(b) and (d)] reveal a gradual decrease in intensities of pre-edge peaks with increase in substitution concentration in both ZFO and ZFAO samples. This is an indication of increase in local structural distortion around the Fe ion with substitution. Similar results are obtained from Zn-edge XANES measurements discussed above and EXAFS results discussed later.

EXAFS study. Oscillations in extended part of absorption spectra relate to inference pattern obtained from local scattering ions of a absorber. Energy dependent absorption coefficient $\mu(E)$ was converted to energy dependent absorption function $\chi(E)$ and thereafter to wave number dependent absorption coefficient $\chi(k)$. Finally, k^2 weighted $\chi(k)$ spectra were Fourier transformed in R space to generate $\chi(R)$ *versus* R (or FT-EXAFS) plots. This data provides information of location of other ions from the center of absorbing atoms. Analysis of EXAFS data has been carried out following standard

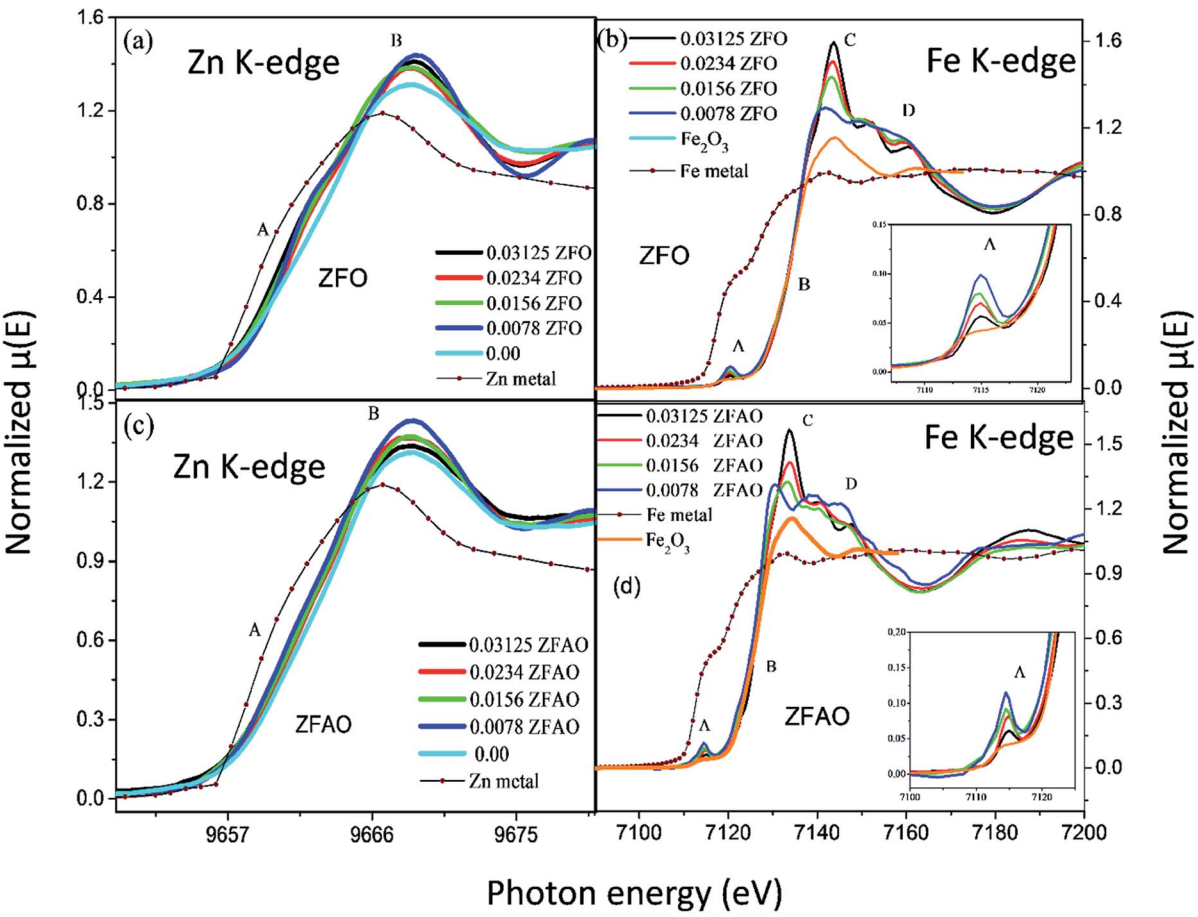

Fig. 5 Normalized absorption spectra ((μ) *vs.* E) at (a) Zn K-edge of ZFO, (b) Fe K-edge of ZFO; "A" and "B" represents absorption edge and white line intensity (c) Zn K-edge of ZFAO and (d) Fe K-edge of ZFAO; "A", "B", "C" and "D" represents pre-edge intensity, absorption edge, white line intensity and structure related interference patterns, respectively.

procedure[46,47] using IFEFFIT software.[48] This includes data reduction, Fourier transforms and generation of refined theoretical fit using FEFF 6.0 code of experimental EXAFS spectra. Starting from a known ideal crystallographic structure, experimental $\chi(R)$ *versus* R data was refined, by modifications of fitting parameters, *i.e.*, oxygen co-ordination number (CN), bond distance (R) between respective atomic pairs and disorder factor (Debye–Waller factor) (σ^2). Debye–Waller factor provides mean square fluctuation in distances and thermal disorder in system.[49] A pure ZnO Wurtzite c structure (space group $p63mc$) with lattice parameters $a = b = 3.22$ Å and $c = 5.16$ Å has been considered.[50] Zn atom is coordinated with 4 oxygen atoms (Zn–O bond ~1.96 Å) in 1st coordination shell. It is also coordinated with 6 Zn atoms in both 2nd and 3rd coordination shells (Zn–Zn distances ~3.18 and 3.20 Å). Fe K-edge data were fitted by considering Zn atoms replaced by Fe atoms in Wurtzite structure. Fitting parameters have been varied independently without defining them by any constraint. Goodness of fit in above process is generally expressed by the R_{factor} which is defined as:

$$R_{\text{factor}} = \sum \frac{[\text{Im}(\chi_{\text{dat}}(r_i) - \chi_{\text{th}}(r_i))]^2 + [\text{Re}(\chi_{\text{dat}}(r_i) - \chi_{\text{th}}(r_i))]^2}{[\text{Im}(\chi_{\text{dat}}(r_i))]^2 + [\text{Re}(\chi_{\text{dat}}(r_i))]^2} \quad (3)$$

where, χ_{dat} and χ_{th} are experimental and theoretical $\chi(R)$ values respectively and Im and Re refer to the imaginary and real parts of respective quantities.

ZFO. k^2 weighted $\chi(k)$ spectra of ZFO samples at both Zn and Fe K-edges have been shifted vertically for better clarity [Fig. 6(a) and (b)]. Spectrum upto 10 Å^{-1} and 9 Å^{-1} at Zn and Fe K-edges respectively was considered for Fourier transform. Refinement was performed in phase uncorrected R-space in range 1–3.5 Å in both cases [Fig. 7(a) and (b)]. Only three single scattering paths have been considered in fitting process (within 1–3.5 Å limit). The 1st intense peak at 1–1.8 Å is due to Zn–O path. Strong 2nd or 3rd peaks convolute at 2.5–3.3 Å corresponding to two Zn–Zn paths. Resemblance of EXAFS data of Zn and Fe-edges of ZFO samples with Zn-edge of pure ZnO ensures proper substitution. Hence, structures of ZFO samples are not distorted enough to deviate from Wurtzite structure. Values of best fit parameters for Zn/Fe edges reveal that average Debye–Waller factor (σ^2) of Zn–O path increases gradually with increase in substitution manifesting an increase in structural disorder upon substitution. Coordination numbers (CN) and bond lengths of pure ZnO sample for all paths (*i.e.* Zn–O, Zn–Zn_s and Zn–Zn_l) are like theoretical values. However, for ZFO samples although Zn–O bond lengths remain steady for most samples, it contracts for $x = 0.03125$. On the other hand, Fe–O bonds are comparable or a little shorter than Zn–O bonds for $x = 0.0078$ but much larger for higher substitutions. This means Fe creates larger shells of oxygen atoms, creating pressure on next shells. This becomes more evident from CN values of Zn–O or Fe–O paths. Average CN for Zn–O path reduces with substitution, while for Fe–O increases. Relative% change of these CN values increases continuously for Fe–O compared to Zn–O up to ~40% in higher substituted samples. Hence, more O is drawn towards Fe than Zn atoms, *i.e.* Fe-site becomes O-rich at the cost of Zn-site becoming O-deficit.

A notable difference is observed between CN values of Zn–Zn and Fe–Zn shells. CN values are lower by 15–30% for Fe–Zn than Zn–Zn paths. This implies that there is ample Zn loss in neighborhood of Fe atoms. Loss is less in case of higher substitutions. At the same time it is observed that both $(\text{Fe–Zn})_s$ and $(\text{Fe–Zn})_l$ bond lengths are shorter than the corresponding $(\text{Zn–Zn})_s$ and $(\text{Zn–Zn})_l$ counterparts. Shorter bonds are ~6–7% while longer ones are 2–7% lesser. This may arise due to availability of space from longer Fe–O bonds than Zn–O. All bond lengths are shorter than bulk materials.[54,55] Values of Zn–O and $(\text{Zn–Zn})_s$ CN's and bond lengths reported here are lower than values reported by Jeong *et al.* (~1.98 Å and ~3.20 Å).[50] $(\text{Zn–Zn})_l$ bond lengths are higher than previously reported results.[51–53] Values of σ^2 Zn–O and Zn–Zn paths for ZFO samples are lower than that of Fe–O and Fe–Zn paths. However, $\sigma^2$of Zn–O and Zn–Zn paths appears to increase nominally with substitution while for Fe–O and Fe–Zn paths it shows decrements in ZFO from pure samples. Hence, disorder is lesser at Zn-site than Fe-site but increases with substitution at the neighborhood of Zn-sites but decreases near Fe-sites. This implies a incremental structural distortion throughout the entire lattice along with condensation of a different structure at local points of vicinity of Fe. This is an indication that structural changes are prone beyond $x = 0.03125$. Such changes may also happen upon provision of thermal energy. Difference between two Zn–Zn bond lengths suggests elongation and contraction of bonds in two different orientations to maintain shell volume. This is a big contrast with previous studies where expansion of bonds happens for all atomic pairs.[56]

ZFAO. k^2 weighted $\chi(k)$ spectra [Fig. 6(c) and (d)] of ZFAO samples and phase uncorrected $\chi(R)$ *vs.* R data [Fig. 7(c) and (d)] fitted with theoretically generated model at Zn and Fe K-edges are plotted. Resemblances between ZFAO, ZFO and ZnO suggest that co-substitution with Ag does not introduce much structural changes in ZFAO samples. Best-fit parameters have been plotted [Fig. 8]. It is reminded that target formula was designed to compensate differences of ionic radii between Fe^{3+}(IV) and Zn^{2+}(IV). Compensation results in stabilization of bond lengths and coordination in ZFAO compared to ZFO. Deviations in Zn–O and Zn–Zn bond lengths of ZFAO samples are lesser than ZFO samples on substitution. CN become more stabilized close to ideal values. Fe–O and Fe–Zn bond lengths too do not vary much. Debye–Waller factor, σ^2 of Zn–O shell decreases gradually upon substitution, showing better structural order at Zn site for ZFAO than ZFO and with better stability. In general, bond lengths, CN and σ^2 of ZFAO matches with ZFO samples. Hence, it may be concluded from these results that Ag incorporation leads to more stable structure with lesser oxygen loss at Zn sites.

Micro-hardness. Effect of structural changes can be related to effects like hardness. Hardness is analyzed in solids by studying their deformation or modification due to a force applied. A general test done to analyze hardness is by indentation method. Area under applied pressure, F (N), in Vickers

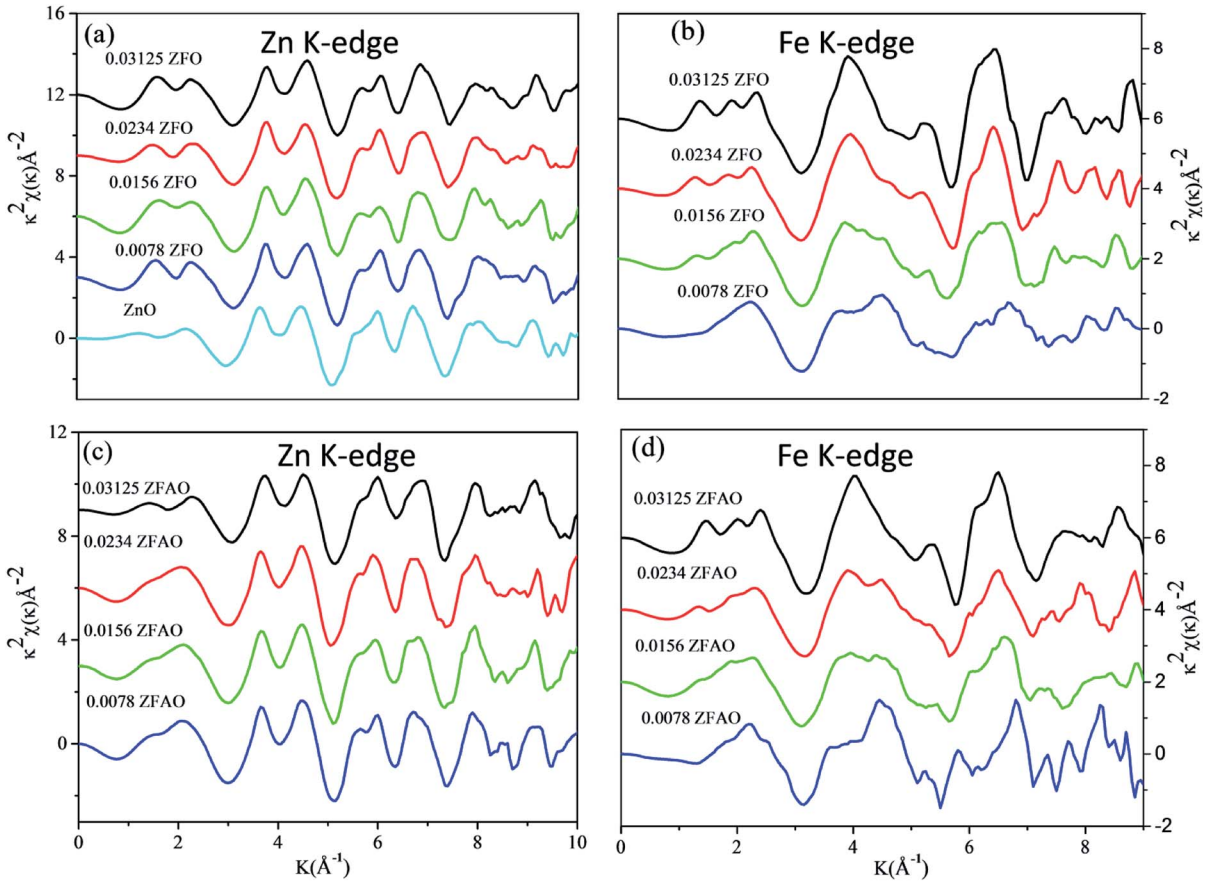

Fig. 6 k^2 weighted $\chi(k)$ spectra at (a) Zn K-edge of ZFO, (b) Fe K-edge of ZFO, (c) Zn K-edge of ZFAO and (d) Fe K-edge of ZFAO.

micro-hardness tester is given by $d^2/2\sin(136^\circ/2) = d^2/1.8544$; where d (μm), calculated using a microscope, is length of diagonals of the trace created by indentation for a definite load. Vickers micro-hardness, H_v, is calculated using, $H_v = (1854.4F/d^2)$ (GPa). In ZFO samples hardness decreased with increasing load [Fig. 9(a)]. This is known as indentation size effect (ISE). Hardness decreased with increasing Fe-substitution as well [Fig. 9(b)]. However, for ZFAO samples a reverse nature is observed. Hardness increased with increasing load and with substitution. This is generally termed as reverse indentation size effect (RISE). Hardness may be related to packing of atoms in a lattice. If a lattice is well packed and not with vacancies then with applied pressure chances of rearrangements are less. However, in presence of vacant sites rearrangements are possible. An estimation of vacant sites can be done from coordination number of constituent elements. It was discussed that CN of Zn–Zn paths reduced with substitution in case of ZFO, while for ZFAO, CN reached a maximum of 6 for both the short and long paths [Fig. 9(c)]. Hence it is evident that in case of ZFAO the lattice becomes extremely regular and hardness increases whereas in ZFO, excess oxygen ions create Zn vacancies which decrease hardness. With increasing load ZFO lattice becomes more and more deformed leading to breaking of bonds and therefore reduction of hardness. On the other hand, in absence of relocation sites ZFAO lattice becomes more compact and difficult to be compressed, thereby increasing hardness.

UV-visible analysis. Bandgap was estimated from extrapolated slopes of energy dependence of optical transmittance data ($(\alpha h\nu)^2$ *vs.* E), with absorption coefficient, α [Fig. 10(a) and (b)]. Band gap initially increased nominally from ~3.20 eV for pure ZnO, to 3.23 eV for $x = 0.0156$ thereafter decreased with further substitution [Fig. 10(c)]. Tailing of band edges is observed. Tailing may be related to lattice strain or defect states created due to hybridization properties of dopant materials. Band tail energy is weakly temperature dependent due to localized states associated with disorder in crystalline materials and is denoted by Urbach energy, E_u.[57–59] E_u can be estimated as:

$$\alpha = \alpha_o \exp(h\nu/E_u) \quad (4)$$

Urbach energy decreases with increase in ZFO and ZFAO incorporation up to $x = 0.0156$, thereafter increases [Fig. 10(d)]; a trend commensurate with bandgap. However, from our EXAFS studies such a behavior is hard to explain. Hence, most probably these defects may be related to new electronic states created near the band edge by dopant ions. Note that the lattice becomes more crystalline with Fe/Ag substitution. This is evident from the strain values calculated from the XRD data as

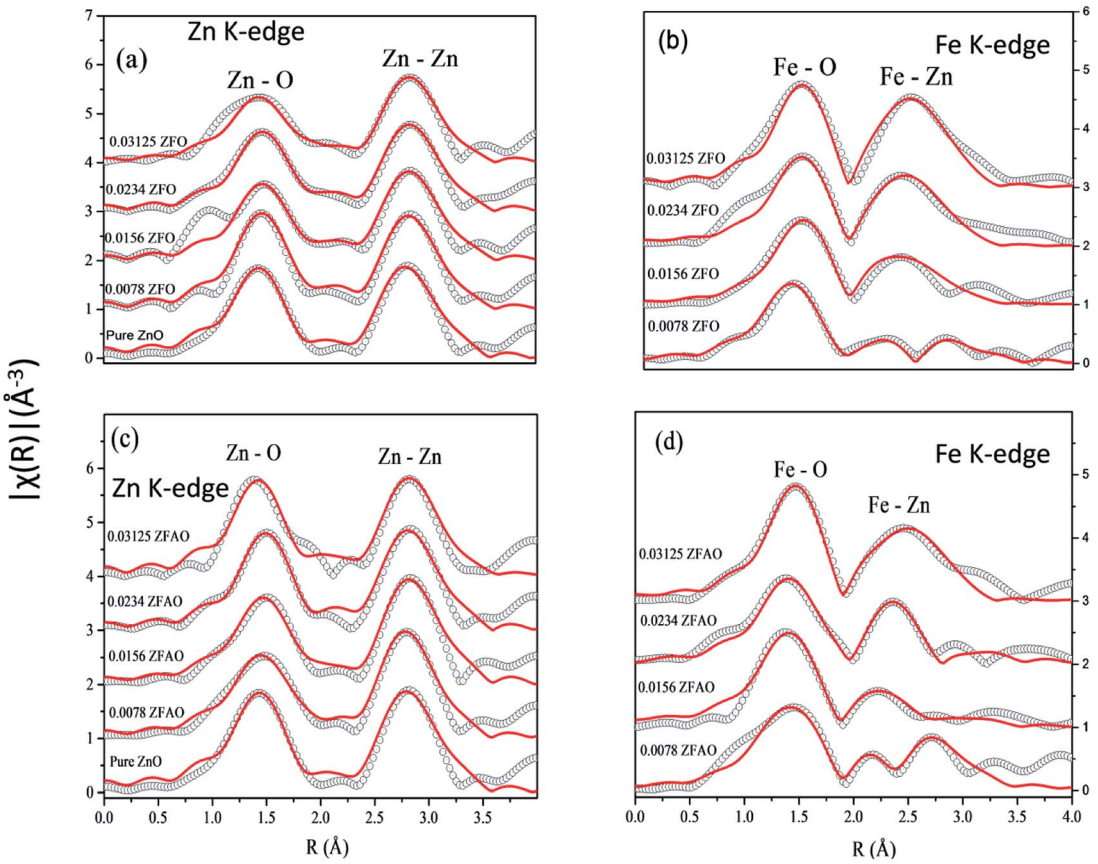

Fig. 7 Theoretically generated $\chi(R)$ *vs.* (R) plot fitted with experimental data (a) Zn K-edge of ZFO, (b) Fe K-edge of ZFO, (c) Zn K-edge of ZFAO and (d) Fe K-edge of ZFAO.

discussed before. Urbach energy is related to lattice strain. Hence, a commensurate behavior between strain and Urbach energy is observed.

Photoluminescence analysis. In general, different defect states are formed inside the bandgap of pure and substituted ZnO. Defect arise due to zinc interstitials ($Zn_i \sim 0.22$ eV),[60] oxygen vacancies ($V_O \sim 2.5$ eV),[61] oxygen interstitials ($O_i \sim 2.28$ eV),[60] and zinc vacancies ($V_{Zn} \sim 2.85$ eV)[61] below the conduction band (CB). Transitions take place from both CB and Zn_i levels to valence band (VB), V_O, O_i and V_{Zn} levels giving rise to several possibilities of different color emissions, such as UV (CB → VB: $\Delta E \sim 3.3$ eV),[60] violet (Zn_i → VB: $\Delta E \sim 3$ eV),[60] blue (CB → V_{Zn}: $\Delta E \sim 2.85$ eV),[61] green (CB → V_O: $\Delta E \sim 2.46$ eV & Zn_i → V_O: $\Delta E \sim$ 2.24 eV),[60–62] yellow (CB → O_i: $\Delta E \sim 2.1$ eV)[61] and orange-red emissions (CB → O_i: $\Delta E \sim 2.28$ eV & Zn_i → O_i: $\Delta E \sim 2.06$ eV).[60] Some of these transitions collectively contribute to a broad spectrum, called Deep Level Emission (DLE) composed of violet (3–3.1 eV), blue (2.50–2.75 eV), green (2.17–2.50 eV), yellow (2.10–2.17 eV), orange-red (<2.1 eV) color ranges. Emissions with energies comparable to bandgap are termed as Near Band Emission (NBE) composed of three regions: UV (~3.16 eV [for donor acceptor pair] and ~3.25 eV [due to free excitons (FX)]) and violet (~3.05 eV).

Room temperature photoluminescence (PL) [Fig. 11(a) and (c)] was studied to understand role of Ag^+ and Fe^{3+} ion in ZnO structure. A sharp NBE centered at ~382 nm is observed. A wider and broader DLE extending from 450 nm to 750 nm is observed in all samples. Relative intensity of DLE keeps on decreasing with substitution while NBE increases. Fig. 12(c) shows the intensities of NBE and DLE that were calculated conventionally. A marked increase in $I_{(NBE)}/I_{(DLE)}$ ratio from 1.13424 for $x = 0.00$ to 3.35 for $x = 0.0156$ is observed in Fe substituted samples and also same trend follows in Fe/Ag samples. For $x > 0.0156$ the ratio decreases in both ZFO and ZFAO [Fig. 12(c)]. An increase in $I_{(NBE)}/I_{(DLE)}$ ratio is related to decrement of defect states[62] and increment in optical transparency of ZnO nano-particles.

Note that DLE of pure ZnO is centered at 500 nm whereas other Fe & Fe/Ag substituted samples are centered at ~530 to 560 nm for $x = 0.0078$ to $x = 0.03125$: a clear red shift in ZFO and ZFAO also. Red shift is more in ZFO than ZFAO. The ZFO PL data (plotted using 1931 standard) further confirms this red shift behavior [Fig. 11(b)]. The values are (0.3177, 0.4427) for pure, (0.4398, 0.4816) for $x = 0.0078$, (0.447, 0.4893) for $x = 0.0156$, (0.514, 0.4613) for $x = 0.0234$ and (0.488, 0.4652) for $x = 0.03125$. Decrement of green emission up to $x = 0.0156$ followed by an enhancement for higher substitution is observed. Chromaticity coordinates of ZFAO PL data (on 1931 standard) [Fig. 11(d)], can be expressed as (0.3177, 0.4427), (0.4224,

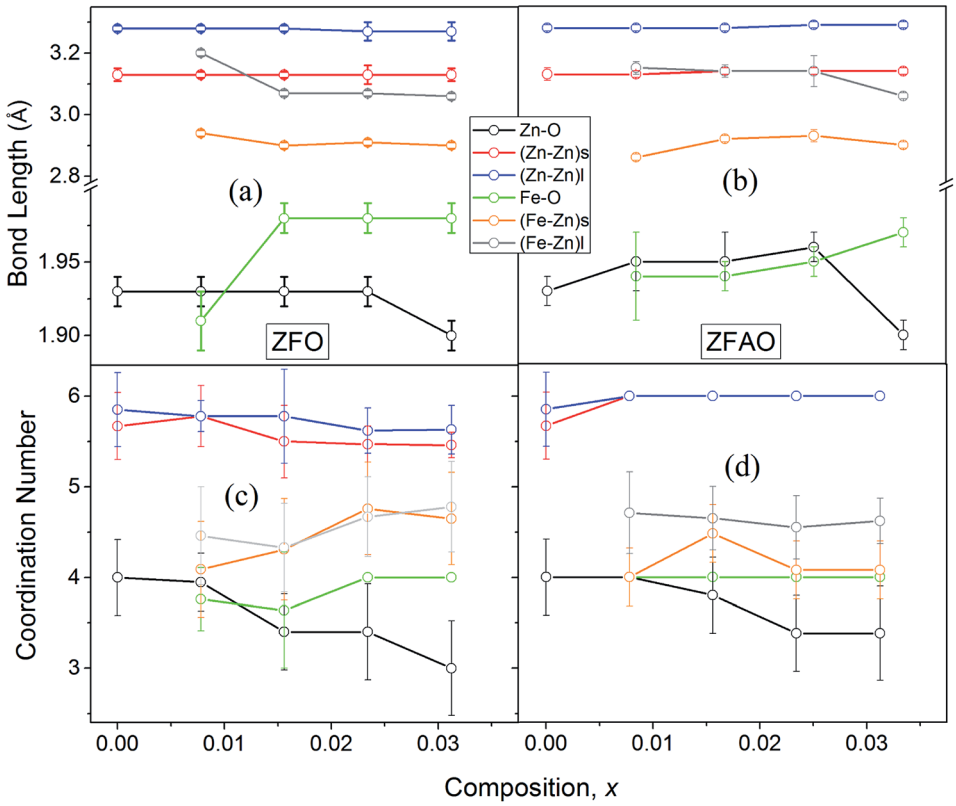

Fig. 8 (a) and (b) Variation of bond lengths of ZFO & ZFAO, (c) and (d) coordination numbers of ZFO & ZFAO with composition (*x*).

0.4774) (0.3898, 0.4807), (0.3342, 0.5123) and (0.3469, 0.5168) in the same order.

PL spectra including both broad DLE as well as NBE were deconvoluted into several peaks belonging to individual colors. Areas were calculated of each fitted peak and added up in groups, A_{UV}, A_V, A_B, A_G, A_Y, A_O, A_R for six color ranges corresponding to UV, violet, blue, green, yellow & orange-red. Contribution of each component color in total spectrum was estimated by calculating color fraction, P_{color}, defined by $P_{color} = A_{color}/A_{total}$, where, $A_{total} = \Sigma A_{color}$, the total area under the

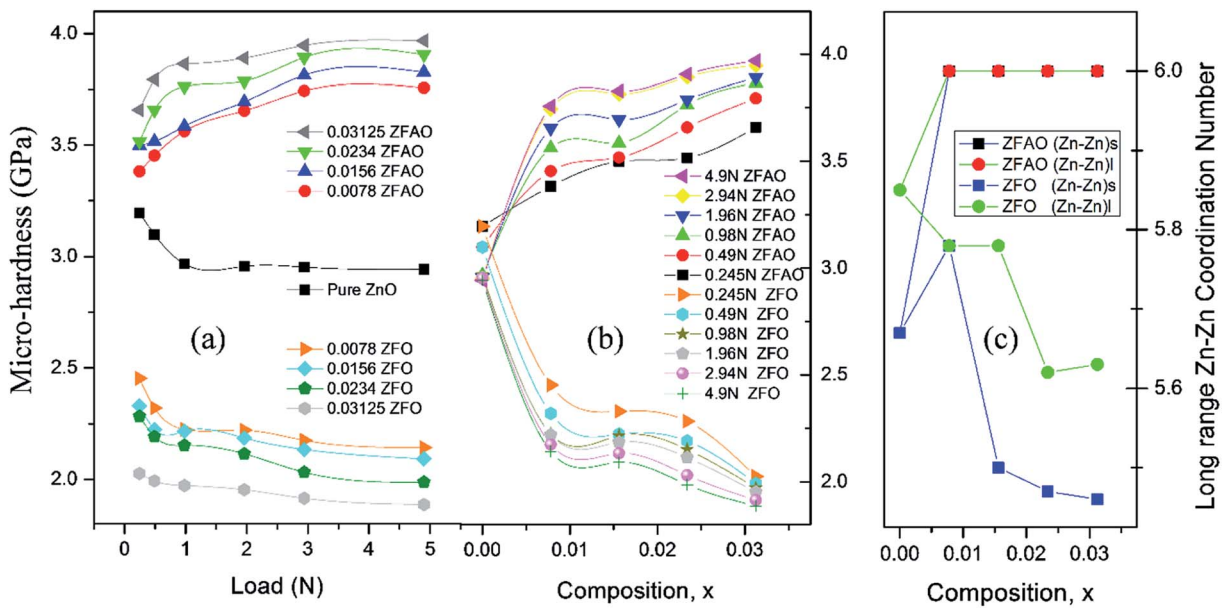

Fig. 9 (a) and (b) Variation of micro-hardness with load (*N*) and composition (*x*), (c) coordination number with composition (*x*).

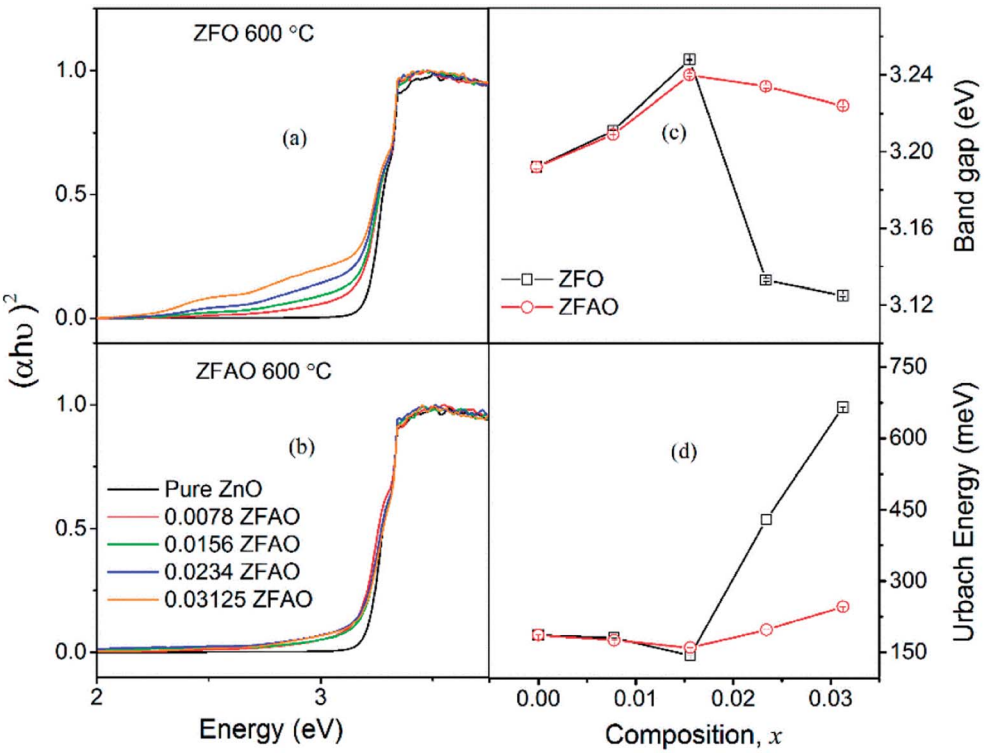

Fig. 10 (a) and (b) Optical transmittance of ZFO & ZFAO, (c) and (d) bandgap and Urbach energy *versus* composition (x).

spectrum. Hence, for each sample $\Sigma P_{color} = 1$. Various defect states in the sample's PL spectrum may be estimated from the color fraction, P_{color}. However, for different compositions A_{total} varies. Although the samples were prepared with care, the total intensity of the PL spectrum may differ for various reasons. Therefore, the sample preparatory factors must be normalized. Being significantly small, the difference in the bandgap and Urbach energies may be neglected. Thus, the total UV emission may be normalized to one and the contribution of all colors from other transitions can be estimated by defining the normalized color fraction, $P_N = P_{color}/P_{UV}$ for each sample.

The NBE of pure ZnO is a contribution of three peaks: UV (3.16 eV [for donor acceptor pair] and 3.25 eV [due to free excitons (FX)]) and violet (3.05 eV); while DLE is a contribution of 9 peaks: blue (2.69 eV), green (2.25 eV, 2.4 eV, and 2.54 eV), yellow (2.08 eV and 2.15 eV) and orange-red range (1.85 eV, 1.95 eV, and 2.02 eV). Similarly, for substituted samples each color range is composed of similar sets of peaks contributing to the same ranges as above.

From composition dependence of P_N, amount of green emission is observed to decrease with increasing substitution up to $x = 0.00156$ in Fe substituted samples; thereafter P_N increases [Fig. 12(b)]. Similar to $I_{(NBE)}/I_{(DLE)}$, the ratio P_{NBE}/P_{DLE} initially increases after that it decreases. [Fig. 12(c)].

Green and red emission decreases in P_N *vs.* x plots upto $x = 0.0156$ followed by increase beyond $x = 0.0156$. This hints at reduction and increment of oxygen vacancy and interstitials with increasing substitution. On the other hand, a similar trend of reduction followed by enhancement of blue and violet emissions indicates similar facts about Zn vacancies and interstitials. Thus Ag^+ and Fe^{3+} substitution, results in initial reduction of defect states, created by Zn and O vacancies and interstitials, up to $x = 0.0156$, followed by increase of all types of defects for $x > 0.0156$. Note that this trend of decrease and increase of defects states is similar to trends in strain and also Urbach energy of these materials.

We observe V_{Zn}/V_O in pure ZnO centered at ~2.5 eV (wavelength 500 nm). When Fe^{3+} incorporates in lattice in ZFO, there is red shift in photoluminescence spectra, that means, reduction in oxygen vacancy but enhances oxygen interstitial defects in that lattice. This implies that lattice is strained and defects are created in system, also supported by EXAFS study. On the other hand, in ZFAO there is size compensation of dopants in lattice and defects are reduced. Hence, Ag^+ plays an important role in reducing defects.

Crystal radius of Ag^+(IV) (~1.14 Å) is bigger than Zn^{2+}(IV) (~0.74 Å). On the other hand, Ag^+, having lower charge, tends to retain less oxygen compared to Zn^{2+}. In Ag-substituted ZnO it has been reported that oxygen defects decrease with Ag^+ incorporation. This is in contrary to what is expected for a substitution by a lesser charged Ag^+. This may happen if Ag^+ions are incorporated as interstitials.[63] Interstitial Ag^+ adds extra charge to lattice. This may attract extra oxygen, thereby reducing oxygen defects. However, Ag^+ being larger in size, lattice cannot accommodate without getting distorted. Hence, interstitials lead to defects and voids.

On the other hand, Fe^{3+}(IV) (~0.63 Å) is smaller than Zn^{2+}. Smaller size and extra positive charge of Fe^{3+} as compared to

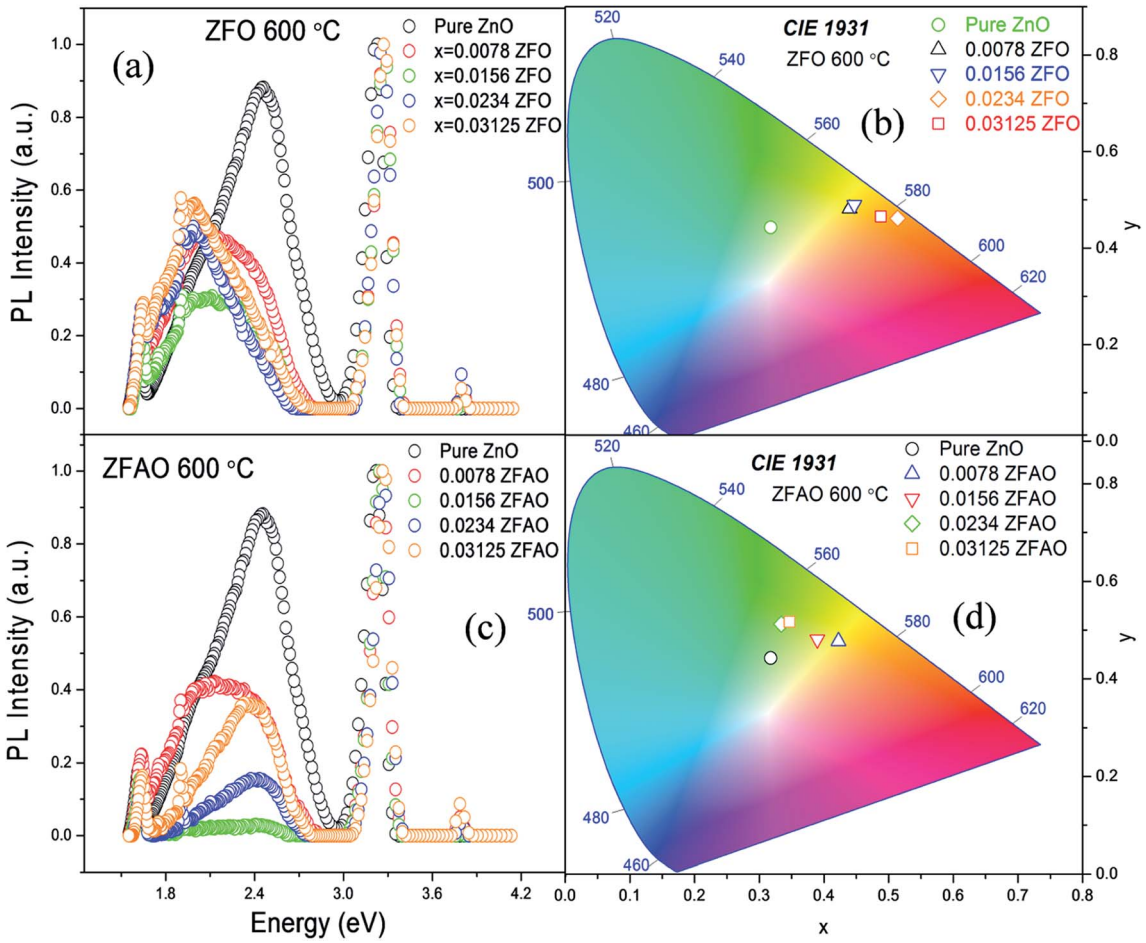

Fig. 11 (a) and (c) PL spectra of ZFO & ZFAO, (b) and (d) chromaticity diagram.

Zn^{2+} attract more oxygen to lattice. Hence, for Fe-substituted ZnO reports show decrement of oxygen defects. However, excess oxygen may lead to oxygen interstitials and thereby lattice distortion. Thus, both Fe^{3+} and Ag^{+} individually, tend to reduce oxygen defects initially. However, increased incorporation of dopant creates lattice distortion and thereby impurity phase.

In $Zn_{(1-x)}Fe_{(0.8x)}Ag_{(0.2x)}O$, *i.e.* Fe : Ag = 4 : 1, was intentionally chosen, so that the combination of bigger Ag^{+} and smaller Fe^{3+} ions can result in an equivalent crystal radii of Zn^{2+}. This helped maintain solubility of dopant elements in the compositions. However, as the proportion of Fe^{3+} is more than Ag^{+} ions, effective added charge is positive. This extra charge helps attract more oxygen to the lattice. Note that the unit cell lattice parameters and volume increase continuously with substitution, in spite ionic size compensation. This is due to addition of more and more oxygen. Initially this takes care of existing oxygen defects inherent in ZnO, which reduces defects and thereby reduce strain and Urbach energy. However, when such defects are compensated, extra oxygen adds as O-interstitials. This further creates Zn vacancies and thereafter structural distortions, causing strain and increase in Urbach energy. Also, Fe-3d electrons hybridize with O-2p electrons and forms intermediate states in between bands[64,65] These defect states also contribute to PL spectrum and thereby have optoelectronic implications.

Magnetization. The hysteresis loops for ZFO and ZFAO measured at 300 K and 10 K are shown in Fig. 13. While pure ZnO exhibits diamagnetic behavior, which is consistent with reported literature[66,67] the Fe and Fe–Ag substituted samples exhibit paramagnetic behavior at 300 K. For both ZFO and ZFAO samples, the paramagnetic interactions are enhanced as the substitution increase. Room temperature paramagnetism has been observed in Co-doped ZnO nanoparticles.[68] The reason for this observation was attributed to the unavailability of free carriers necessary for ferromagnetic interactions. The absence of RTF in our ZFO and ZFAO samples may be attributed to the same reason. The hysteresis loops of the substituted samples measured at 10 K apparently demonstrate superparamagnetic behavior (see insets of Fig. 13c and (d)), where the magnetization doesn't saturate even at 50 kOe for any of the samples. However, a close look at the low field regions of the loops show coercivity (H_c) and remanence magnetization (M_r) indicating the presence of weak ferromagnetic interactions in the compounds.

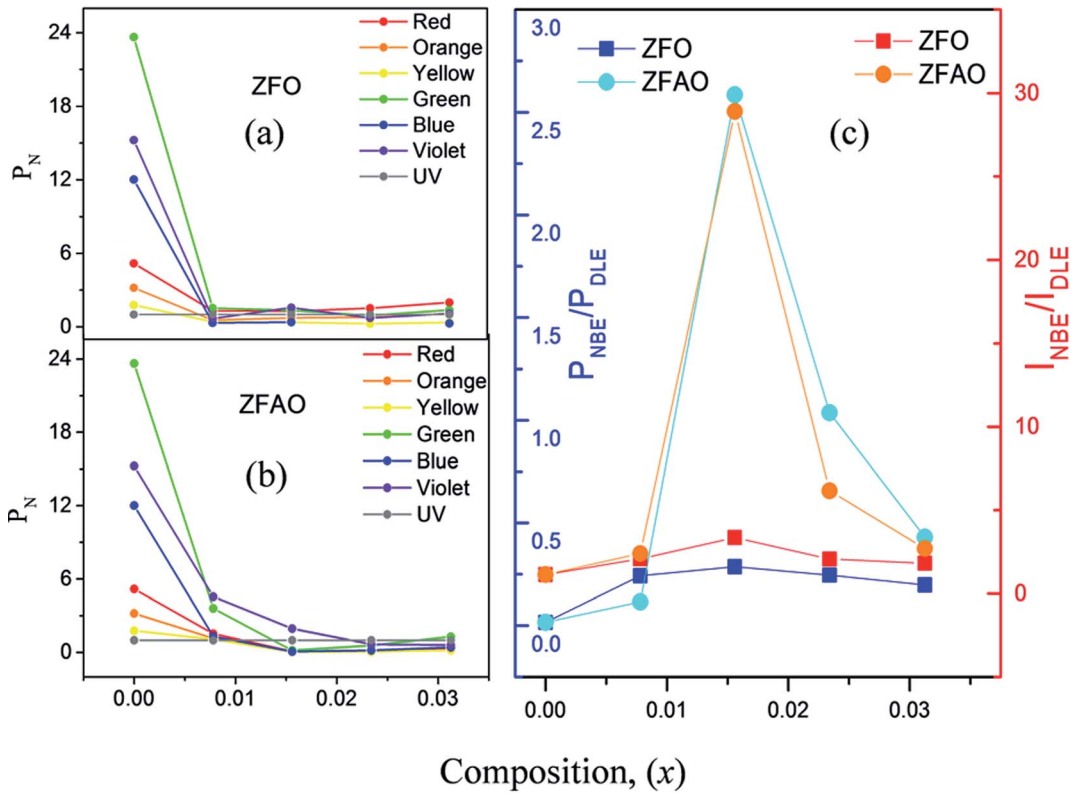

Fig. 12 (a) and (b) P_N of ZFO & ZFAO with respect to composition (x), (c) I_{NBE}/I_{DLE} and P_{NBE}/P_{DLE} with respect to composition (x).

The hysteresis loops of the substituted samples measured at 10 K [shown in Fig. 13(c) and (d)] shows that the magnetization is not saturated even at 50 kOe for any of the samples. However, a close look at the low field regions of the loops show coercivity (H_c) and remanence magnetization (M_r) indicating the presence of weak ferromagnetic interactions in the compounds. The H_c linearly increase from ~132 Oe ($x = 0.0078$) to ~148 Oe ($x = 0.03125$) for ZFO and from ~143 Oe ($x = 0.0078$) to ~200 Oe ($x = 0.03125$) for ZFAO. Although H_c in both series are reasonably significant, the M_r for the samples are small. In case of ZFO, a maximum M_r of 0.028 emu g^{-1} is observed for $x = 0.03125$ and for the same concentration a maximum M_r of 0.05 emu g^{-1} is observed in ZFAO. The magnetization at 50 kOe range between 0.3 emu g^{-1} and 1.36 emu g^{-1} for ZFO and between 0.27 emu g^{-1} and 1.18 emu g^{-1} for ZFAO.

A ferromagnetic exchange interaction between Fe^{3+} and other ions may give rise to ferromagnetic properties observed in our samples. A longer ferromagnetic exchange can be mediated by polaronic percolation of bound magnetic polarons formed by point defects like oxygen vacancies.[69,70] Ag incorporation in ZFAO increases the oxygen vacancies and therefore they exhibit relatively stronger ferromagnetism (as evident in their higher H_c and M_r) in comparison to ZFO. These observations suggest that although presence of ferromagnetism is evident in both ZFO and ZFAO at 10 K, superparamagnetism is dominant in the materials. Such coexistence of ferromagnetism and superparamagnetism has been observed by other researchers in Co-doped ZnO samples.[67]

Goktas *et al.* have reported RTF in Fe and Al co-doped ZnO nanostructured thin films.[71] The RTF in their samples significantly depended on the annealing temperature. Goktas *et al.* also studied a series of $Zn_{1-x}Fe_xO$ films and observed ferromagnetism at 5 K an 100 K in the film with $x = 0.2$.[72] At higher temperatures the film showed diamagnetic behavior. For $x \leq 0.10$ all their samples showed paramagnetic behavior at all temperatures. $Zn_{0.95}Co_{0.05}O$ nanoparticles prepared by sol–gel method demonstrate paramagnetism at room temperature, while thin films of same composition deposited by pulsed laser deposition method showed superparamagnetic behavior at room temperature.[67,68] These observations and proposed explanations mentioned in the literature suggest that the magnetic properties of substituted ZnO are extremely sensitive to defects that may vary with growth conditions. Even in absence of defects, a long-range ferromagnetic coupling may happen from interactions mediated by delocalized Zn-s states resulting in super- and double-exchange.[73] As discussed earlier, Ag^+ ions help to minimize zinc interstitial defects and stabilize structure. Better structural uniformity in ZFAO than ZFO may help in a better long range ferromagnetic coupling. Also, V_O seems to be reduced due to extra charge of Fe^{3+}. Hence, in these samples it seems a long range ferromagnetic coupling mediated through a hybridization involving Zn-s states may be instrumental to yield a very weak ferromagnetism in substituted samples which enhances upon better structural ordering.

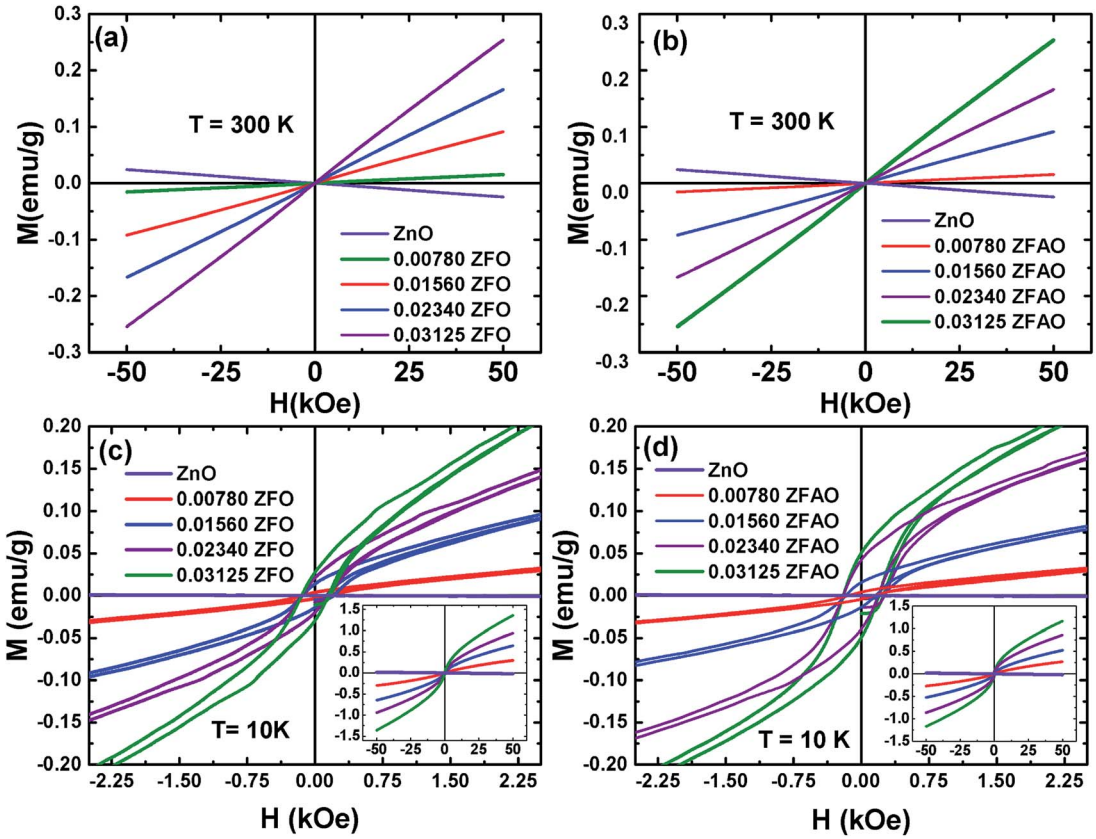

Fig. 13 Hysteresis loops (M–H) of ZFO & ZFAO measured at 300 K and 10 K. The insets of (c) and (d) show the complete hysteresis loops measured between −50 kOe and 50 kOe.

Conclusion

Structural, optical and magnetic properties of sol–gel prepared hexagonal, wurtzite $Zn_{(1-x)}Fe_{(x)}$ O and $Zn_{(1-x)}$-$Fe_{(0.8x)}Ag_{(0.2x)}O$ nanoparticles, of size ~48–80 nm have been studied. Substituting of Fe results in the decrease of lattice constants in ZFO while the lattice expands due to the co-doping of Fe and Ag in ZFAO. EXAFS studies confirm changes in local coordination of Zn atoms, which affects mechanical properties of these materials. While Fe-substitution reduces hardness of ZFO, Ag addition to the Fe-substituted lattice further strengthens the lattice. This may be related to excess oxygen addition to lattice being attracted by additional charge of Fe^{3+}. For both systems, defects, strain and Urbach energy reduce with substitution up to $x = 0.0156$ probably due to reduction in inherent Zn-interstitials and O-vacancies. However, with further substitution and excess oxygen in lattice internal strain increases creating defects. Fe 3d–O 2p hybridization creates states inside bandgap which are further contributions to strain beyond $x = 0.0156$. Bandgap, photoluminescence follows same trend. XANES study clearly rules out presence of metallic Fe clusters, FeO and Fe_2O_3 phases in samples. However, it indicates that Fe gets incorporated in the ZnO lattice as mix charge state in Fe^{2+}/Fe^{+3} causing reduction of oxygen vacancies. These observations corroborate to those of EXAFS study. Coercive field and remnant magnetization studies also hint at proper substitution. For such a homogeneous lattice solution, some ferromagnetic ordering is evident at very low temperature which is enhanced by Ag^{+} addition. This may be due to some Zn-s state facilitated long range exchange mechanism.

Conflicts of interest

There are no conflicts of interest to declare.

Acknowledgements

Authors thank Dr Vipul Singh at IIT, Indore, for providing Photoluminescence Spectroscopy. We also thank Sophisticated Instrumentation Center (SIC), IIT Indore for Scanning Electron Microscopy and IIT Indore for funding the project. Authors are grateful to Dr Kaushik for providing UV/vis facility in INST Mohali. We would like to thank Dr Anand Parey, Solid Mechanics lab, Department of Mechanical Engineering at IIT Indore. Authors wish to thank Mr Sandeep Patil for his help in performing Vickers micro-indentation measurements. One of the authors (Dr Sajal Biring) acknowledges financial support from the Ministry of Science and Technology (Grant No. MOST105-2218-E-131-003 and 106-2221-E-131-027).

References

1 U. Özgür, Y. I. Alivov, C. Liu, A. Teke, M. A. Reshchikov, S. Doğan, V. Avrutin, S.-J. Cho and H. Morkoç, *J. Appl. Phys.*, 2005, **98**, 041301.

2 H. Zeng, W. Cai, P. Liu, X. Xu, H. Zhou, C. Klingshirn and H. Kalt, *ACS Nano*, 2008, **2**, 1661–1670.

3 H. Zeng, X. Xu, Y. Bando, U. K. Gautam, T. Zhai, X. Fang, B. Liu and D. Golberg, *Adv. Funct. Mater.*, 2009, **19**, 3165–3172.

4 M. H. Huang, *Science*, 2001, **292**, 1897–1899.

5 P. Srivastava and Y. Sharma, *Adv. Mater. Lett.*, 2011, **2**, 290–293.

6 D. A. Schwartz and D. R. Gamelin, *Adv. Mater.*, 2004, **16**, 2115–2119.

7 H. Zhou, J. Fallert, J. Sartor, R. J. B. Dietz, C. Klingshirn, H. Kalt, D. Weissenberger, D. Gerthsen, H. Zeng and W. Cai, *Appl. Phys. Lett.*, 2008, **92**, 132112.

8 B. Xiang, P. Wang, X. Zhang, S. A. Dayeh, D. P. R. Aplin, C. Soci, D. Yu and D. Wang, *Nano Lett.*, 2007, **7**, 323–328.

9 G. D. Yuan, W. J. Zhang, J. S. Jie, X. Fan, J. A. Zapien, Y. H. Leung, L. B. Luo, P. F. Wang, C. S. Lee and S. T. Lee, *Nano Lett.*, 2008, **8**, 2591–2597.

10 U. K. Gautam, L. S. Panchakarla, B. Dierre, X. Fang, Y. Bando, T. Sekiguchi, A. Govindaraj, D. Golberg and C. N. R. Rao, *Adv. Funct. Mater.*, 2009, **19**, 131–140.

11 T. Dietl, H. Ohno, F. Matsukura, J. Cibert and D. Ferrand, *Science*, 2000, **287**, 1019–1022.

12 K. Sato and H. Katayama-Yoshida, *Jpn. J. Appl. Phys.*, 2001, **40**, L555.

13 T. Fukumura, Z. Jin, A. Ohtomo, H. Koinuma and M. Kawasaki, *Appl. Phys. Lett.*, 1999, **75**, 3366–3368.

14 B. Panigrahy, M. Aslam and D. Bahadur, *Nanotechnology*, 2012, **23**, 115601.

15 M. V. Limaye, S. B. Singh, R. Das, P. Poddar and S. K. Kulkarni, *J. Solid State Chem.*, 2011, **184**, 391–400.

16 G. Glaspell, P. Dutta and A. Manivannan, *J. Cluster Sci.*, 2005, **16**, 523–536.

17 J. Iqbal, B. Wang, X. Liu, D. Yu, B. He and R. Yu, *New J. Phys.*, 2009, **11**, 063009.

18 V. K. Sharma and G. D. Varma, *Adv. Mater. Lett.*, 2012, **3**, 126–129.

19 A. Goktas, I. H. Mutlu, Y. Yamada and E. Celik, *J. Alloys Compd.*, 2013, **553**, 259–266.

20 A. Goktas, I. H. Mutlu and Y. Yamada, *Superlattices Microstruct.*, 2013, **57**, 139–149.

21 C. N. R. Rao and F. L. Deepak, *J. Mater. Chem.*, 2005, **15**, 573.

22 J. Alaria, H. Bieber, S. Colis, G. Schmerber and A. Dinia, *Appl. Phys. Lett.*, 2006, **88**, 112503.

23 S. Kolesnik and B. Dabrowski, *J. Appl. Phys.*, 2004, **96**, 5379–5381.

24 M. A. Garcia, J. M. Merino, E. Fernandez Pinel, A. Quesada, J. De La Venta, M. L. Ruiz Gonzalez, G. R. Castro, P. Crespo, J. Liopis, J. M. Gonzalez-Calbet and A. Hernando, *Nano Lett.*, 2007, **7**, 1489.

25 H. Li, Y. Huang, Q. Zhang, Y. Qiao, Y. Gu, J. Liu and Y. Zhang, *Nanoscale*, 2011, **3**, 654–660.

26 X. Qiu, L. Li, C. Tang and G. Li, *J. Am. Chem. Soc.*, 2007, **38**, 11908.

27 B. S. Reddy, S. V. Reddy and R. P. V. Lakshmi, *Optoelectron. Adv. Mater., Rapid Commun.*, 2012, **6**, 953.

28 M. He, Y. F. Tian, D. Springer, I. A. Putra, G. Z. Xing, E. E. M. Chia, S. A. Cheong and T. Wu, *Appl. Phys. Lett.*, 2011, **99**, 222511.

29 A. J. Chen, X. M. Wu, Z. D. Sha, L. J. Zhuge and Y. D. Meng, *J. Phys. D: Appl. Phys.*, 2006, **39**, 4762–4765.

30 A. Singhal, S. Achary, A. Tyagi, P. Manna and S. Yusuf, *Mater. Sci. Eng., B*, 2008, **153**, 47–52.

31 A. H. Shah, M. B. Ahamed, E. Manikandan, R. Chandramohan and M. Iydroose, *J. Mater. Sci.: Mater. Electron.*, 2013, **24**, 2302–2308.

32 M. Zarbali, A. Göktaş, I. H. Mutlu, S. Kazan, A. G. Şale and F. Mikailzade, *J. Supercond. Novel Magn.*, 2012, **25**, 2767–2770.

33 A. Goktas, *Appl. Surf. Sci.*, 2015, **340**, 151–159.

34 W. Zhang, J. Zhao, Z. Liu and Z. Liu, *Appl. Surf. Sci.*, 2013, **284**, 49–52.

35 X. X. Wei, C. Song, K. W. Geng, F. Zeng, B. He and F. Pan, *J. Phys.: Condens. Matter*, 2006, **18**, 7471–7479.

36 V. Ghafouri, A. Ebrahimzad and M. Shariati, *Sci. Iran.*, 2013, **20**, 1039–1048.

37 H. S. Chin and L. S. Chao, *J. Nanomater.*, 2013, **2013**, 1–8.

38 M. Saleem, L. Fang, A. Wakeel, M. Rashad and C. Y. Kong, *World J. Condens. Matter Phys.*, 2012, **2**, 10–15.

39 J. Yang, *Sensors*, 2013, **13**, 2719–2734.

40 J. Yang, X. Liu, L. Yang, Y. Wang, Y. Zhang, J. Lang, M. Gao and B. Feng, *J. Alloys Compd.*, 2009, **47**, 632–635.

41 S. Basu, C. Nayak, A. K. Yadav, A. Agrawal, A. K. Poswal, D. Bhattacharyya, S. N. Jha and N. K. Sahoo, *J. Phys.: Conf. Ser.*, 2014, **493**, 012032.

42 A. K. Poswal, A. Agrawal, A. K. Yadav, C. Nayak, S. Basu, S. R. Kane, C. K. Garg, D. Bhattacharyya, S. N. Jha and N. K. Sahoo, *AIP Conf. Proc.*, 2014, **1591**, 649–651.

43 B. S. Reddy, S. V. Reddy, N. K.Reddy and Y. P. Reddy, *Adv. Mater. Lett.*, 2014, **5**, 199–205.

44 J. Wong, F. W. Lytle, R. P. Messmer and D. H. Maylotte, *Phys. Rev. B*, 1984, **30**, 5596–5610.

45 A. K. Rana, Y. Kumar, P. Rajput, S. N. Jha, D. Bhattacharyya and P. M. Shirage, *ACS Appl. Mater. Interfaces*, 2017, **9**, 7691–7700.

46 D. C. Konigsberger and R. Prince, *X-Ray Absorption: Principles, Applications, Techniques of EXAFS, SEXAFS and XANES*, Edited book Wiley, New York, 1988.

47 S. D. Kelly, D. Hesterberg, B. Ravel, A. L. Ulery and L. R. Drees, *SSSA Book Series Methods of Soil Analysis Part 5—Mineralogical Methods*, 2008, vol. 5, pp. 387–464.

48 M. Newville, B. Ravel, D. Haskel, J. Rehr, E. Stern and Y. Yacoby, *Phys. Rev. B: Condens. Matter Mater. Phys.*, 1995, **208**, 154–156.

49 E. H. Kisi and M. M. Elcombe, *Acta Crystallogr., Sect. C: Struct. Chem.*, 1989, **45**, 1867–1870.

50 E. S. Jeong, H. J. Yu, Y. J. Kim, G. C. Yi, Y. D. Choi and S. W. Han, *J. Nanosci. Nanotechnol.*, 2010, **10**, 3562.
51 S. Kumar, S. Basu, B. Rana, A. Barman, S. Chatterjee, S. N. Jha, D. Bhattacharyya, N. K. Sahoo and A. K. Ghosh, *J. Mater. Chem. C*, 2014, **2**, 481–495.
52 T. Chakraborty, C. Meneghini, G. Aquilanti and S. Ray, *J. Phys.: Condens. Matter*, 2013, **25**, 236002.
53 S. Kumar, N. Tiwari, S. N. Jha, S. Chatterjee, D. Bhattacharyya, N. K. Sahoo and A. K. Ghosh, *RSC Adv.*, 2015, **5**, 94658–94669.
54 A. K. Yadav, R. Dey, R. Bhunia, S. Hussain, S. N. Jha, D. Bhattacharyya, R. Bhar and A. K. Pal, *J. Polym. Res.*, 2016, **23**, 265.
55 E.-S. Jeong, H.-J. Yu, S.-W. Han, S. J. An, J. Yoo, Y.-J. Kim and G.-C. Yi, *J. Korean Phys. Soc.*, 2008, **53**, 461–465.
56 Z. Wu, Y. Zhou, X. Zhang, S. Wei and D. Chen, *Appl. Phys. Lett.*, 2004, **84**, 4442–4444.
57 A. Abdelkrim, S. Rahmane, O. Abdelouahab, A. Hafida and K. Nabila, *Chin. Phys. B*, 2016, **25**, 046801.
58 S. Benramache, B. Benhaoua and F. Chabane, *J. Semicond.*, 2012, **33**, 093001.
59 N. Chahmat, A. Haddad, A. Ain-Souya, R. Ganfoudi, N. Attaf and M. Ghers, *J. Mod. Phys.*, 2012, **03**, 1781–1785.
60 B. Cao, W. Cai and H. Zeng, *Appl. Phys. Lett.*, 2006, **88**, 161101.
61 B. Lin, Z. Fu and Y. Jia, *Appl. Phys. Lett.*, 2001, **79**, 943–945.
62 C. H. Ahn, Y. Y. Kim, D. C. Kim, S. K. Mohanta and H. K. Cho, *J Appl. Phys.*, 2009, **105**, 089902.
63 S. Hosseini, I. A. Sarsari, P. Kameli and H. Salamati, *J. Alloys Compd.*, 2015, **640**, 408–415.
64 J. Papierska, A. Ciechan, P. Bogusławski, M. Boshta, M. M. Gomaa, E. Chikoidze, Y. Dumont, A. Drabińska, H. Przybylińska, A. Gardias, J. Szczytko, A. Twardowski, M. Tokarczyk, G. Kowalski, B. Witkowski, K. Sawicki, W. Pacuski, M. Nawrocki and J. Suffczyński, *Phys. Rev. B*, 2016, **94**, 224414.
65 J. J. Beltrán, C. A. Barrero and A. Punnoose, *Phys. Chem. Chem. Phys.*, 2015, **17**, 15284–15296.
66 J. Wang, J. Wan and K. Chen, *Mater. Lett.*, 2010, **64**, 2373.
67 Q. Li, Y. Wang, L. Fan, J. Liu, W. Kong and B. Ye, *Scr. Mater.*, 2013, **69**, 694–697.
68 A. Sivagamasundari, R. Pugaze, S. Chandrasekar, S. Rajagopan and R. Kannan, *Appl. Nanosci.*, 2013, **3**, 383.
69 A. Kaminski and S. D. Sarma, *Phys. Rev. Lett.*, 2002, **88**, 247202.
70 L. Bergqvist, O. Eriksson, J. Kudrnovský, V. Drchal, P. Korzhavyi and I. Turek, *Phys. Rev. Lett.*, 2004, **93**, 137202.
71 A. Goktasa, F. Aslana, B. Yeşilatab and İ. Boza, *Mater. Sci. Semicond. Process.*, 2018, **75**, 221–233.
72 A. Goktas, I. H. Mutlu and Y. Yamada, *Superlattices Microstruct.*, 2013, **57**, 139–149.
73 L. Hedin and B. I. Lundqvist, *J. Phys. C: Solid State Phys.*, 1971, **4**, 2064–2083.